Investigation of Theoretical Solutions to a Bottom-Raised Oscillating Surge Wave Energy Converter (OSWEC) Through Experimental and Parametric Studies

Preprint

Nhu Nguyen,[1] Jacob Davis,[2] Krish Thiagarajan,[3] Nathan Tom,[4] and Salman Husain[4]

1 Sandia National Laboratories
2 University of Washington
3 University of Massachusetts Amherst
4 National Renewable Energy Laboratory

**NREL is a national laboratory of the U.S. Department of Energy
Office of Energy Efficiency & Renewable Energy
Operated by the Alliance for Sustainable Energy, LLC**

Conference Paper
NREL/CP-5700-85083
July 2023

This report is available at no cost from the National Renewable Energy Laboratory (NREL) at www.nrel.gov/publications.

Investigation of Theoretical Solutions to a Bottom-Raised Oscillating Surge Wave Energy Converter (OSWEC) Through Experimental and Parametric Studies

Preprint

Nhu Nguyen,[1] Jacob Davis,[2] Krish Thiagarajan,[3] Nathan Tom,[4] and Salman Husain[4]

1 Sandia National Laboratories
2 University of Washington
3 University of Massachusetts Amherst
4 National Renewable Energy Laboratory

INVESTIGATION OF THEORETICAL SOLUTIONS TO A BOTTOM-RAISED OSCILLATING SURGE WAVE ENERGY CONVERTER (OSWEC) THROUGH EXPERIMENTAL AND PARAMETRIC STUDIES

Nhu Nguyen
Sandia National Laboratories
Albuquerque, NM

Jacob Davis
University of Washington
Seattle, WA

Krish Thiagarajan
University of Massachusetts
Amherst, MA

Nathan Tom
National Renewable Energy Laboratory
Golden, CO

Salman Husain
National Renewable Energy Laboratory
Golden, CO

ABSTRACT

Experiments were conducted on a wave tank model of a bottom raised oscillating surge wave energy converter (OSWEC) model in regular waves. The OSWEC model shape was a thin rectangular flap, which was allowed to pitch in response to incident waves about a hinge located at the intersection of the flap and the top of the supporting foundation. Torsion springs were added to the hinge in order to position the pitch natural frequency at the center of the wave frequency range of the wave maker. The flap motion as well as the loads at the base of the foundation were measured. The OSWEC was modeled analytically using elliptic functions in order to obtain closed form expressions for added mass and radiation damping coefficients, along with the excitation force and torque. These formulations were derived and reported in a previous publication by the authors. While analytical predictions of the foundation loads agree very well with experiments, large discrepancies are seen in the pitch response close to resonance. These differences are analyzed by conducting a sensitivity study, in which system parameters, including damping and added mass values, are varied. The likely contributors to the differences between predictions and experiments are attributed to tank reflections, standing waves that can occur in long, narrow wave tanks, as well as the thin plate assumption employed in the analytical approach.

Keywords: OSWEC, analytical, hydrodynamic coefficients, RAO, foundation forces.

1. INTRODUCTION

Oscillating surge wave energy converters (OSWEC) leverage the elliptical trajectories of the water wave particles which flatten horizontally as waves transition from deep to shallow water depths [1-3]. Linear potential theory has been widely used to model OSWECs, notably the Oyster device, an OSWEC-type device that was deployed offshore of Orkney, Scotland [2,4-6].

Wei et al. conducted a computational fluid dynamics (CFD) analysis of an OSWEC device and remarked that linear potential theory models can produce close matches to the experimental tests and CFD simulations [7-8]. They also investigated vortex shedding at the edges of the device and viscous drag effects and found that the radiation and diffraction effects dominate viscous effects.

While a substantial body of work exists on the use of linear potential theory to model OSWECs (see [4-5; 9]),Wei et al. caution against ignoring viscous effects altogether as the non-linear effects such as overtopping and slamming can result in errors in motion calculations. Further, Babarit et al. reckoned that the miscalculation of viscous drag effects could be the foremost source of errors and can result in overestimating the power yield estimation by as much as 30% [7,10]. In addition to discrepancies in power generation, linear potential theory models may overestimate response near resonance [11-13].

The current study seeks to validate the analytical modeling of an experimentally tested prototype of a bottom-raised OSWEC. The experimental tests were conducted under the Technology Commercialization fund of the U.S. Department of Energy to support a collaboration between the National Renewable Energy Laboratory and University of Massachusetts Amherst [14]. The OSWEC device discussed here is mounted on a raised platform or is `bottom-raised', as opposed to other designs with the hinge axis directly at the seafloor [3,6,9,15]. The bottom-raised configuration uses a mounting structure that allows a wider range of deployment sites that may be in deeper seas while keeping the device close to the water surface.

The analytical approach employed in this study was previously presented by Nguyen et al. and Davis [16,17]. Theoretical formulas were developed to evaluate the hydrodynamic coefficients (added mass and radiation damping) of an OSWEC using flat plate assumptions in elliptical coordinates, the OSWEC's response amplitude operators (RAOs) in pitch motion, as well as the foundational forces/torques in surge and pitch directions. This work further examines the performance and limitations of this analytical approach through parametric study to emulate the experimentally observed behavior. The parameter tuning process is carried out by varying the hydrodynamics coefficients for the

radiation field effects (i.e., added mass and radiation damping) by up to ±50%.

The rest of the paper is organized as follows: Section 2 describes the equations of motion of the OSWEC – specifically its Response Amplitude Operator, and the relevant structural loads; Section 3 describes the experimental setup, and Section 4 describes the experimental results; Section 5 compares the analytical simulations against the experimentally measured system responses, which is followed by the parametric studies that tune added-mass and radiation damping in Section 6. Finally, the conclusions are made in Section 7.
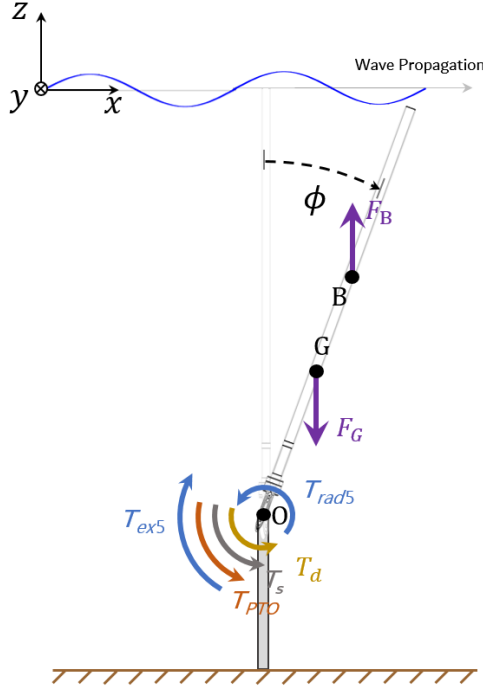

FIGURE 1 – Torques on the OSWEC body

2. THEORETICAL MODEL

For completeness, this section briefly described the governing equations employed in the theoretical modeling tool. Readers are referred to [17] for details of the formulas along with their derivations. It is noted that the effect of the power take-off (PTO) on the system physics is not considered in this study.

The OSWEC is constrained to move only in the pitch direction. The general one degree of freedom equation of motion derived from the sum of torques is

$$I_{55}\ddot{\phi} = T_{ex5} + T_{rad5} + T_G + T_B + T_s + T_d \quad (1)$$

where I_{55} is the pitch moment of inertia and $\ddot{\phi}$ is the second time derivative of the pitch displacement ϕ, or the pitch angular acceleration. T_G and T_B are gravity and buoyancy torques, respectively, which produce counteracting moments about the hinge O (Fig. 1). T_{ex5} and T_{rad5} denote excitation and radiation torque in the pitch direction of motion. Additional torques, resulting from the PTO (T_{PTO}), external springs (T_s), and viscous sources (T_d), also contribute to moment about the hinge.

In the case of regular, monochromatic waves, the incident wave elevation is described by linear wave theory as

$$\eta(x,t) = \Re\{ae^{i(\omega t - kx)}\} \quad (2)$$

where a is the wave amplitude, or half the wave height H, i is the imaginary unit, ω is the angular frequency, and k is the wavenumber.

The torques on the right-hand side of Equation (1) can now be expressed as functions of frequency as [18, 19]

$$T_{ex5}(\omega) = \Re\{aX_5(\omega)e^{i\omega t}\} \quad (3)$$

$$T_{rad5}(\omega) = \Re\{-\omega^2 A_{55}(\omega)\tilde{\phi}e^{i\omega t} + i\omega B_{55}(\omega)\tilde{\phi}e^{i\omega t}\} \quad (4)$$

where X_5 is the frequency-dependent complex pitch excitation torque, comprising of an ordinary amplitude $|X_5|$ and phase $\angle X_5$. The radiation torque, on the other hand, is represented as the linear sum of the added mass and radiation damping contributions, which are in phase with the OSWEC angular acceleration and velocity, respectively. Here A_{55} is the frequency-dependent pitch added moment of inertia and B_{55} is the pitch radiation damping coefficient. The torque contributions due to gravity and buoyancy are combined to obtain a net hydrostatic torque as [19]

$$T_{hs}(\omega) = C_{55}\phi(t) = \Re\{C_{55}\tilde{\phi}e^{i\omega t}\} \quad (5)$$

with

$$C_{55} = \rho V r_b - m r_g \quad (6)$$

Here the mass and volume of the OSWEC are denoted by m and V, and the lever arms for buoyancy and gravitational forces by r_b, r_g respectively. The coefficients are grouped into a hydrostatic restoring coefficient, denoted C_{55}, and the *sine* term is linearized under the assumption that, for small pitch displacements, $\sin(\phi(t)) \approx \phi(t)$.

The remaining two torque contributions, which account for externally attached springs and viscous damping sources, are described as

$$T_s(\omega) = \Re\{C_{ext}\tilde{\phi}e^{i\omega t}\} \quad (7)$$

$$T_d(\omega) = \Re\{i\omega B_v\tilde{\phi}e^{i\omega t}\} \quad (8)$$

where C_{ext} is the net restoring coefficient of any externally attached springs and B_v is the net damping coefficient, comprising of any viscous sources which can be approximated as linearly proportional to the pitch angular velocity. The latter will be approximated here through system identification and will be discussed in subsequent sections.

2

The expressions in Equations (3)-(8) are substituted into the general equation of motion Equation (1), and rearranged to obtain the frequency domain equation of motion as

$$\tilde{\phi}\big[-\omega^2\big(I_{55} + A_{55}(\omega)\big) + i\omega(B_{55} + B_{PTO} + B_v) \\ + (C_{55} + C_{PTO} + C_{ext})\big] = aX_5(\omega) \qquad (9)$$
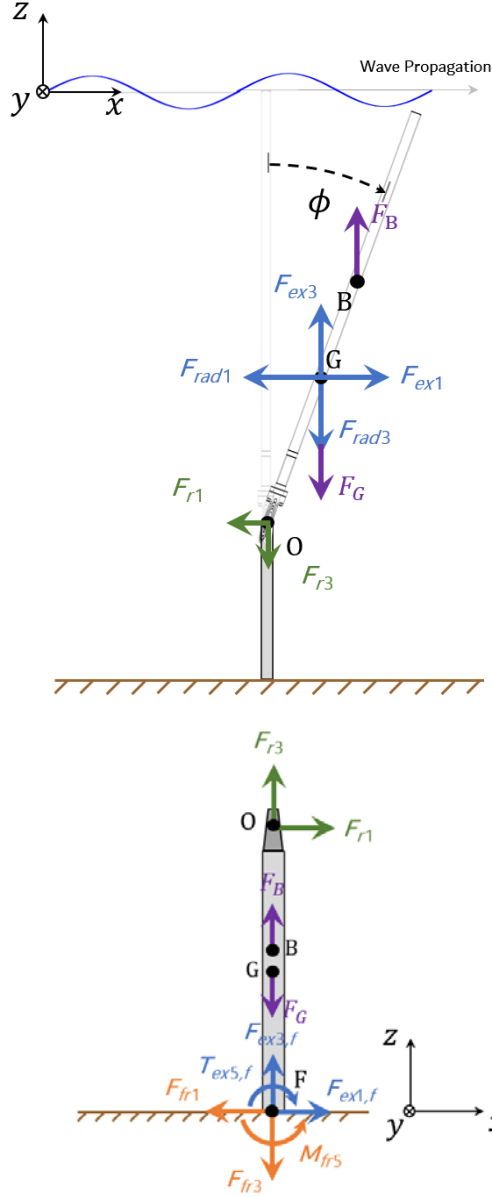
2.1 Response Amplitude Operator

The RAO represents the transfer function between the OSWEC (pitch) motion and the incident wave amplitude. For

waves in the linear regime, it provides a prediction of the OSWEC pitch response for any wave period and amplitude combination. It is derived simply from the rearrangement of the frequency domain equation of motion (Equation (9)) as

$$RAO \equiv \frac{\tilde{\phi}}{a} = \frac{X_5(\omega)}{[-\omega^2 A^* + i\omega B^* + C^*]} \qquad (10)$$

with

$$A^* = \big(I_{55} + A_{55}(\omega)\big) \qquad (11)$$
$$B^* = B_{55}(\omega) + B_{PTO} + B_v \qquad (12)$$
$$C^* = C_{55} + C_{PTO} + C_{ext} \qquad (13)$$

The RAO is commonly non-dimensionalized by the wave number of the incident wave

$$RAO^* \equiv \frac{\tilde{\phi}}{ka} \qquad (14)$$

where an asterisk has been used to distinguish the non-dimensional quantity from its dimensional counterpart. The RAO will be integral to characterizing and understanding the OSWEC dynamics in subsequent sections.

2.2 Hinge Reaction Forces

Neglecting centrifugal forces, the surge and heave reaction forces, F_{r1} and F_{r3}, at the hinge (point O in Fig. 2) of a fore-aft symmetrical OSWEC can be described in the frequency domain following [20] as

$$F_{r1}(\omega) = (-\omega^2 A_{15} + i\omega B_{15})\tilde{\phi} - aX_1 \qquad (15)$$
$$F_{r3}(\omega) = -(\rho V - m) - aX_3 \qquad (16)$$

where A_{15} and B_{15} are the surge-pitch added mass and surge-pitch radiation damping coefficients, respectively. X_1 and X_3 denote the complex surge and heave excitation forces, respectively. The surge reaction force is composed entirely of dynamic terms that result from the motion of the OSWEC itself, and the incident wave load. The heave reaction force, on the other hand, is composed of a static contribution from the net hydrostatic forces and a time-varying wave load component. Due to the flat plate assumption, the heave reaction force, however, is not calculated in the analytical study.

2.3 Hydrodynamic coefficients

Analytical calculations of RAO and hinge reaction forces/torques require evaluations of added mass and damping coefficients including A_{55}, A_{15}, B_{55}, and B_{15}. As mentioned previously, closed-form expressions for these parameters have been proposed in the authors' previous work [16] by solving Laplace's equation of an oscillating flat plate in an elliptical coordinate system (Helmholtz equation). The general solutions to the Helmholtz equation are then obtained employing the angular Mathieu and Hankel-Mathieu equations. For completeness, the derived formulas of these terms are summarized in Equations (17)-(22)

$$A_{55} = \rho w^2 \pi \sum_{n=0}^{\infty} f_n^2 \, Im\left\{\sum_{m=0}^{\infty} \frac{B_1^{(2m+1)^2} No_{2m+1}(0,\tau)}{4Ho_{\xi\,2m+1}^{(1)}(0,\tau)}\right\} \qquad (17)$$

FIGURE 2 – (Top) Forces at the hinge O. (Bottom) Foundation force and torque balance.

$$B_{55} = -\rho \omega w^2 f_o^2 \pi \, Re\left\{\sum_{m=0}^{\infty} \frac{B_1^{(2m+1)^2} No_{2m+1}(0,\tau)}{4Ho_{\xi_{2m+1}}^{(1)}(0,\tau)}\right\} \quad (18)$$

$$A_{15} = \rho w^2 \pi \sum_{n=0}^{\infty} f_n \lambda_n \, Im\left\{\sum_{m=0}^{\infty} \frac{B_1^{(2m+1)^2} No_{2m+1}(0,\tau)}{4Ho_{\xi_{2m+1}}^{(1)}(0,\tau)}\right\} \quad (19)$$

$$B_{15} = -\rho \omega w^2 f_o \lambda_o \pi \, Re\left\{\sum_{m=0}^{\infty} \frac{B_1^{(2m+1)^2} No_{2m+1}(0,\tau)}{4Ho_{\xi_{2m+1}}^{(1)}(0,\tau)}\right\} \quad (20)$$

Where

$$f_n = \frac{\sqrt{2}[k_n(h-c)\sinh k_n h + \cosh k_n c - \cosh k_n h]}{k_n^2 \left(h + \left(\frac{g}{\omega^2}\right)\sinh^2 k_n h\right)^{\frac{1}{2}}} \quad (21)$$

$$\lambda_n = \frac{\sqrt{2}(\sinh k_n h - \sinh k_n c)}{k_n \left(h + \frac{g}{\omega^2}\sinh^2 k_n h\right)^{\frac{1}{2}}} \quad , \quad n = 0,1,2,3,\dots \quad (22)$$

Here, $Ho^{(1)}$ and No are called the odd Hankel-Mathieu of the first kind and radial Mathieu functions of the second kind with order m, respectively. Ho_ξ is the derivative of Ho with respect to ξ. B_1 refers to the first coefficient associated with se functions, which is called the odd Mathieu functions. Definitions of other parameters are described in Table 1.

2.4 Foundation Shear Force and Bending Moment

Treating the foundation as its own hydrodynamic body that is rigidly fixed to the sea bottom, the force balances and torques about point F at the base of the foundation are

$$\sum F_x = F_{ex1,f} + F_{fr1} + F_{r1} \quad (23)$$
$$\sum F_z = F_{ex3,f} + F_{fr3} + F_{r3} + F_G + F_B \quad (24)$$
$$\sum T^F = T_{ex5,f} + M_{fr5} + r_f F_{r1} \quad (25)$$

where $F_{ex1,f}$ and $F_{ex3,f}$ are the foundation surge excitation and heave excitation forces, respectively (distinguished from those of the OSWEC body through the use of the f subscript); $T_{ex5,f}$ is the foundation pitch excitation torque; F_{fr1}, F_{fr3}, and M_{fr5} are the foundation reaction forces/torques in the surge, heave, and pitch directions, respectively; $r_f \equiv \overline{FO}$ represents the distance from the base of the foundation F to the hinge point O; and F_G and F_B are the gravitational and buoyancy forces on the foundation, separate from those of the OSWEC body force balance. Contrary to the OSWEC body, the foundation does not experience any radiation hydrodynamic loads, as it does not undergo any rigid body motion. F_{r1} and F_{r3} are the equal but opposite hinge reaction forces introduced in the OSWEC force balance (Equations (15) and (16)). These forces and torques are summarized in Fig. 2.

3. EXPERIMENTAL STUDY

An experimental campaign was conducted at the Ocean Resources and Renewable Energy (ORRE) laboratory at University of Massachusetts Amherst. This section discusses the prototype sizing and construction, sensor instrumentation, and experimental setup of the OSWEC system. The test matrix and data post-processing procedures are also described.

3.1 Model Design

The experimental OSWEC was designed at the tank scale to make best use of the available space in the ORRE wave tank test section. The cross section of the tank's test section is approximately 1.2 m wide with a nominal water depth of 1 m. The following objectives were targeted throughout the sizing process:

- The top of the OSWEC should be flush with the mean water line at its mean position.
- Effects from the tank walls on the hydrodynamics of the OSWEC should be minimized; sufficient clearance should be left on either side of the model to enable flow to pass relatively freely.
- The OSWEC should be stable in the unperturbed configuration. This requires the hydrostatic restoring coefficient, C_{55}, to be greater than zero.
- The net balance of the weight and buoyancy forces, F_G and F_B, should be minimized such that the vertical force on the hinge is near zero when the paddle is submerged to its design depth.

The final dimensions and properties of the scale OSWEC used in the experiments are summarized in Tables 1 and 2. Readers are referred to [17] for details on the selection of the dimensions, inertial properties, and hydrostatic properties of the prototype.

Table 1 - Primary dimensions of the experimental OSWEC

Symbol	Dimension	Value	Unit
h	Water depth	1.000	m
H_o	Height	0.500	m
w	Width	0.400	m
p	Thickness	0.076	m
r_g	Hinge to center of gravity	0.175	m
r_b	Hinge to center of buoyancy	0.284	m
$r_{g,B}$	Hinge to ballast center of gravity	0.082	m
z_h	Hinge depth (from MWL*)	0.534	m
y_w	Wall clearance (once side)	0.400	m
H_g	Gap between the OSWEC and top of the foundation	0.089	m
H_f	Foundation height	0.411	m
D_f	Foundation diameter	0.133	m
z_f	Foundation depth, measured from MWL to top	0.569	m

*MWL: mean water line

3.2 Scaled Model Fabrication

A scale OSWEC model was built to the dimensions shown in Table 1. The top, base, and sides of the model body were cut from 12.5 mm (1/2 in.) acrylic bar stock. 6.25 mm (1/4 in.) acrylic sheet was used for the fore and aft faces. The entire assembly was connected to a 12.5 mm (1/2 in.) stainless steel shaft rigidly fixed to the aluminum support frame. Upper and lower ballast ports were included to provide flexibility in the center of gravity and moment of inertia. The tilt sensor, used to track the motion of the body, was fixed to the top of the body through a stainless steel bracket, sized to elevate the sensor above the maximum expected water elevation and oriented to have a minimal effect on the hydrodynamics. A six-axis load cell was installed at the base of the assembly to record the shear and bending moments at the base of the foundation during experimentation.

Table 2 - Properties of the experimental OSWEC

Symbol	Property	Value	Unit
m_O	Body mass	6.40	kg
m_B	Ballast mass	7.92	kg
M	Total mass	14.32	kg
V	Displaced volume	0.0155	m^3
I_{55}	Moment of inertia about hinge *	0.855	$kg\text{-}m^2$
I_{55}^G	Moment of inertia about center of gravity	0.414	$kg\text{-}m^2$
C_{55}	Hydrostatic restoring coefficient *	18.54	$kg\text{-}m^2\,s^{-2}$
C_{ext}	External torsion spring restoring coefficient **	**0**, 56	$kg\text{-}m^2\,s^{-2}$
T_n	Natural period **	**4.22**, 1.76	s
ω_n	Natural frequency **	**1.49**, 3.57	rad/s
$\|F_B\| - \|F_G\|$	Net hydrostatic vertical force	11.57	N

* Indicating the calculation point has been omitted from the symbol to remain consistent
with the derivations throughout the text. Unless otherwise noted, the properties used in the figures and equations are calculated about the hinge, point O.
** Two experimental configurations were used: the OSWEC with **no external attachments** and the OSWEC with external torsion springs.

To capture the hydrodynamics due to the presence of a monopile foundation beneath the OSWEC, a rigid, 0.133 m (5.25 in.) diameter acrylic tube was integrated into the support structure (Fig. 3). The tube was secured to the center beam through a stainless steel threaded rod to isolate the tube from contacting the lower part of the frame. Once lifted down into the tank, the acrylic tube was allowed to flood with water. It is noted here that the experimental OSWEC includes a cylindrical tube, as the foundational support, whereas the boundary conditions of the analytical model are representative of a wall-like foundation with a width equivalent to that of the OSWEC itself.

FIGURE 3 – OSWEC scaled model. (Left) OSWEC fabricated mode. (Right) Foundational tube assembly with the six-axis load cell installed at the base.
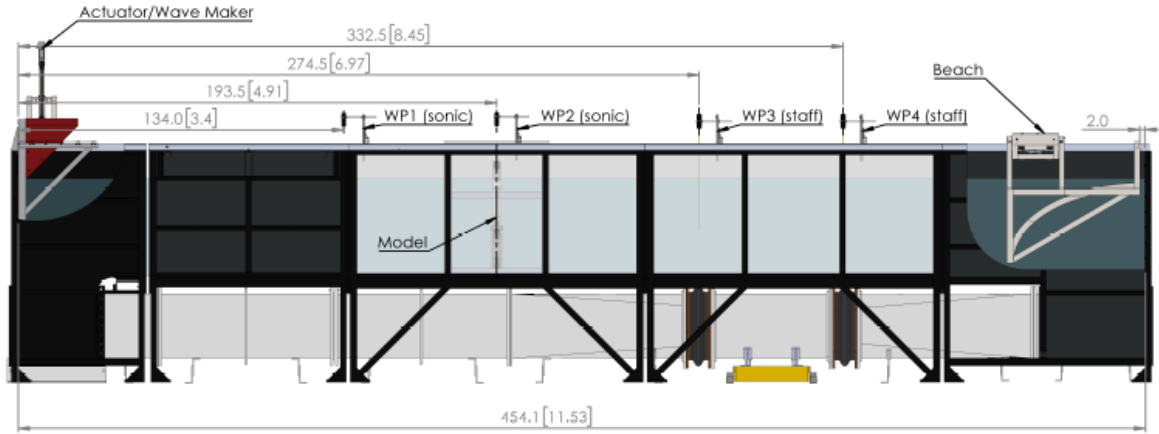
3.3 Wave Tank Configuration

The OSWEC model and its support frame were centered in the test section of the ORRE wave flume, a distance 193.5 in. (4.91 m) from the start of the tank. Four wave probes (abbreviated WP1–WP4 in subsequent figures and discussion) were set up along the length of the tank: WP1, a sonic probe, was placed ahead of the model at a distance of 134 in. (3.4 m); WP2, another sonic probe, was placed overhead the model location at 193.5 in.; WP3, a capacitive staff, was placed behind the model at 274.5 in. (6.97 m); and WP4, a capacitive staff, was placed just ahead of the beach at 332.5 in. (8.45 m). WP1, WP3, and WP4 were centered laterally in the tank throughout the duration of the experiments. WP2 was also centered in the tank during the design wave calibration but was offset laterally to be centered in the 0.413 m gap between one side of the model and the tank wall during model runs. A schematic of the wave tank configuration is presented in Fig. 4.

3.4 Test Matrix

Two model configurations were used in the experiments: 1) the OSWEC with no external springs; and 2) the OSWEC with external torsional springs, added to observe the dynamics of the OSWEC at its natural frequency. These two configurations will be labeled and stylized as no external springs **and external springs** in subsequent figures and discussion. Both configurations employed the 0.133m (5.25 in.) diameter acrylic tube designed to mimic a monopile foundation.

Free decay experiments were performed for each configuration to observe the natural frequency and for later tuning of the analytical models. Initial pitch displacements of approximately 5 to 25 degrees were observed. All the design waves used in the experiments were regular, first order waves

5

FIGURE 4 – Wave tank configuration; Breakout sections have been included to reveal the location of the wavemaker and beach; units: in. [m.]

(monochromatic waves). The wave periods spanned the wave maker capabilities, ranging from 0.8 s to 2.8 s. A target steepness of H/L=0.0035 was set, resulting in amplitudes from 1.5 mm to 14.3 mm. Each design wave and model experiment run lasted for 60 s: the wavemaker began operation at 0 s with a 3 s ramp time and ended operation at 40 s. 20 s of additional time was allotted before the sensor readings stopped. The design waves were calibrated at the location of the model (193.5 in from the start of the tank). The wave amplitudes were calculated as the mean amplitude of three runs, where the individual amplitudes were determined from the Fourier transform of a 30 s wave elevation time history recorded by WP2.

On average, the standard deviation of the three runs was 0.60 % of the mean value. The highest standard deviation to mean ratio was 3%, observed for the smallest wave condition with an amplitude of 1.25 mm. A target number of 1-2 runs was set for each model run wave condition (repeated for both model configurations), except for the 1.3 s and 2.0 s conditions, which were repeated five times to better quantify the repeatability of the experiments. It is noted that these two periods were chosen at random to test the repeatability. They carry no special characteristics compared to other periods. The periods, wavemaker actuator amplitudes, calibrated wave amplitude mean and standard deviations, and target number of runs for each condition are summarized in Table 3.

3.5 Post-processing

Following data collection, signals from the wave probes, tilt sensor, and load cell were trimmed into 30 s records, leaving out the first 10 s of each run to remove transient motions from the model and wavemaker. For each signal, a Fast Fourier Transform (FFT) was used to roughly identify the peak frequency, and a fourth-order Butterworth low-pass filter, with the cutoff frequency set to a value five times this peak frequency, was applied. If higher harmonics (e.g., due to wave reflection) with an amplitude at least 25% of the peak were present in the FFT, the cutoff frequency was instead set to 5 times higher than this value. Following filtering, each signal was further trimmed to obtain an integer number of cycles and a final FFT was

performed to identify the amplitude and frequency from the largest peak. This process was repeated for each experimental run. If multiple runs of the same experimental configuration and wave condition were available, the period and amplitude were recorded as the mean of the combined results. If more than two runs were present, a standard deviation was calculated. This methodology applies to all frequency-domain experimental values reported in the following results and discussion.

Table 3 – Test matrix

T (s)	Actuator Amp (mm)	a_{mean}* (mm)	a_{std}* (mm)	Target No. Runs (#)
0.8	1.25	1.5	0.05	1-2
1.0	3.75	3.0	0.02	1-2
1.3	16.75	4.5	0.02	5
1.6	15.00	6.5	0.06	1-2
1.7	16.50	6.1	0.01	1-2
1.8	18.75	7.9	0.11	1-2
1.9	20	6.0	0.01	1-2
1.95	23	4.9	0.01	1-2
2.0	26	5.2	0.01	5
2.05	29	7.5	0.02	1-2
2.1	32.5	10.3	0.02	1-2
2.2	35	10.6	0.01	1-2
2.4	40	10.1	0.02	1-2
2.6	42	13.1	0.06	1-2
2.8	80	14.3	0.11	1-2

* Calculated from FFT of 3 independent runs

4. EXPERIMENTAL RESULTS

4.1 System Identification

Experimental free-decay responses were used to perform system identification on both OSWEC configurations. This process ensured the accurate representation of the physical OSWEC by the analytical models. The system parameters of interest include estimates of the linear viscous damping, and the natural period (or natural frequency). As part of the study, the

6

quadratic damping term was also calculated and presented here for reference.

To approximate the viscous (or linear) damping, a standard logarithmic decrement method was performed on each free decay run. The logarithmic decrement, which represents the rate at which the damped free response amplitude decays, is obtained from two successive peaks of the response as [21]

$$\delta = \frac{1}{n}\ln\frac{\phi_k}{\phi_{k+n}} \tag{26}$$

where ϕ_k and ϕ_{k+n} are peaks occurring n cycles apart beginning at the kth oscillation cycle. This expression is related to the damping ratio, ζ, by

$$\zeta = \frac{1}{\sqrt{1+\left(\frac{2\pi}{\delta}\right)^2}} \tag{27}$$

The equation above can also be rearranged to get

$$\frac{\zeta}{\sqrt{1-\zeta^2}} = \frac{1}{2\pi}\delta = \frac{1}{2\pi}\frac{1}{n}\ln\frac{\phi_k}{\phi_{k+n}} \tag{28}$$

Meanwhile, to better characterize the damping in the system, a theoretical approach to approximating both a viscous (linear) and quadratic damping coefficient from a hydrodynamic free-decay response was also adopted from [23]. A quadratic damping term is first introduced into the equation of motion as

$$T_{d,quad} = C_D\dot{\phi}|\dot{\phi}| \tag{29}$$

where C_D is the quadratic damping coefficient, including the projected area and water density. If the decayed oscillation is assumed to be approximately sinusoidal over one-half cycle, the quadratic velocity term can be linearized using a Fourier series expansion:

$$\dot{\phi}|\dot{\phi}| \approx \frac{8}{2\pi}\omega_n\phi_k\dot{\phi} \tag{30}$$

The linearized damping force term can be written as [24]

$$\zeta = \frac{B_{55}+B_v+B_{PTO}}{2(I_{55}+A_{55})\omega_n} + \frac{4}{3\pi}\frac{C_D}{(I_{55}+A_{55})}\phi_k \tag{31}$$

In Equation (31), on the right-hand side, the first term represents the linear damping part while the second term quantifies the quadratic damping component. The current study does not consider PTO, hence, $B_{PTO} = 0$. Employing Equations (26) and (27) from logarithmic decrement approach, ζ can be calculated for both no spring and **external springs** cases (Tables 4 and 5). From the results, ζ is calculated to be in the range of 0.1, which indicates $\zeta^2 \ll 1$, and Equation (28) can be simplified as

$$\zeta = \frac{1}{2\pi}\frac{1}{n}\ln\frac{\phi_k}{\phi_{k+n}} \tag{32}$$

Equating Equations (28) and (29) and if peaks from oscillation cycles spaced two periods apart are considered, we get

$$\frac{1}{2\pi}\frac{1}{2}\ln\frac{\phi_{k-1}}{\phi_{k+1}} = \zeta = \frac{B_{55}+B_v}{2(I_{55}+A_{55})\omega_n} + \frac{4}{3\pi}\frac{C_D}{(I_{55}+A_{55})}\phi_k \tag{33}$$

The expression in Equation (33) is fit with the quantity on the left-hand side as the dependent variable and ϕ_k as the independent variable. The resulting intercept represents the linear damping part, and the slope, m, is directly related to the quadratic drag coefficient. The results in this part together with I_{55} (from experiment), A_{55}, and B_{55} (calculated from the

analytical model employed in the current study), B_v and C_D can be estimated.

Results from the free-decay experiments, which are conducted with different initial displacements, are presented in Table 4 (no external springs) and Table 5 (**external springs**). The natural period estimates were obtained from the difference of adjacent peaks, ϕ_k and ϕ_{k+1}, averaged over all the positive and negative peaks separated by 1 period ($n = 1$). Bulk linear and quadratic damping coefficients were obtained from collating the dependent and independent variables of Equation (33) for every run of each configuration. The fits are presented in Fig. 5.

Table 4 – Free decay results, no external springs

ϕ_o (deg)	ω_n (rad/s)	T_n (s)	ζ (-)
-10.4	1.58	3.97	0.096
-11.6	1.55	4.05	0.093
-16.3	1.51	4.16	0.088
-15.3	1.52	4.14	0.096
-10.4	1.57	4.01	0.097

Table 5 – Free decay results, **external springs**

ϕ_o (deg)	ω_n (rad/s)	T_n (s)	ζ (-)
-24.4	3.62	1.74	0.106
-21.4	3.67	1.71	0.110
-17.3	3.54	1.77	0.095
-16.1	3.58	1.76	0.088
-29.8	3.54	1.77	0.110
-25.2	3.58	1.76	0.112
-6.8	3.91	1.61	0.082
-16.0	3.72	1.69	0.099
-11.8	3.67	1.71	0.090

For both the no-external and external springs cases, average values of ζ are taken. Employing Equation (33) in combination with the hydrodynamic coefficients evaluated at the natural frequency, the viscous and quadratic damping coefficients were calculated from the intercept and the slope of the fit lines as $B_v = 0.316, 0.850$ (no springs, **springs**); and $C_D = 4.788, 5.221$ (no springs, **springs**).

4.2 Pitch Response and Response Amplitude Operator

The pitch response signals recorded by the tilt sensor were post-processed to obtain the frequency-dependent pitch amplitude, $|\phi|$. When normalized by the incident wave amplitude to produce an estimate of the response amplitude operator, the response can provide valuable insight into the dynamics of an OSWEC design. Typically, a sharp peak in the RAO will be present at the natural frequency. The amplitude of this peak is determined by the magnitude of the damping. This region generally corresponds to a frequency range where the highest

7

loads are observed, and in the case of power extraction, the frequency at which the available power is maximized [22].
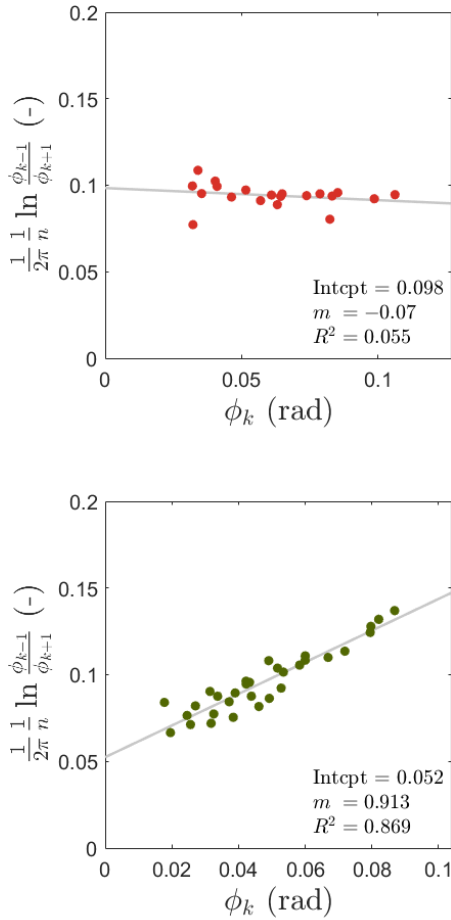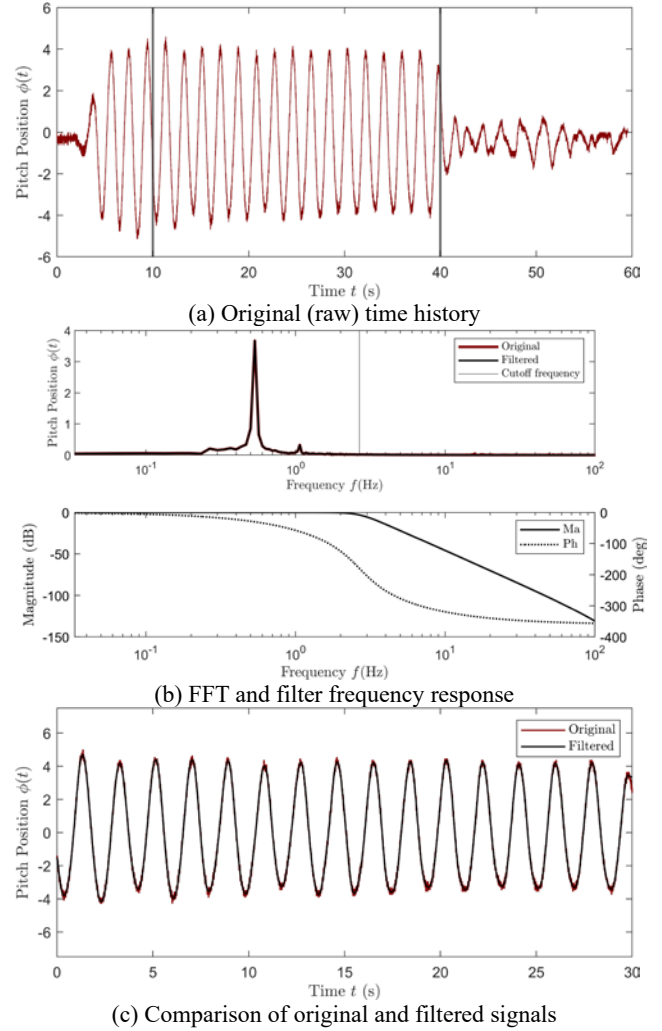

FIGURE 5 - Quadratic damping fits. Top: no spring. Bottom: with **external springs**. Here, ϕ_k is the peak of the kth oscillation cycle, ϕ_{k-1} is the peak occurring one cycle behind, and ϕ_{k+1} is the peak occurring one cycle ahead ($n = 2$). Intercept (Intcpt), slope, and R^2 value for bulk results are displayed.

4.3 Pitch Response Sample Results

A typical pitch response time history and the accompanying post-processing figures are shown in Fig. 6 for $T = 1.9\ s$. Note the smaller, but not insignificant, FFT peak at 1.25 Hz; this is likely a 2nd harmonic of the wave attributed to reflections from the beach at the far end of the wave tank.

The formation of an additional irregularity can also be seen below this frequency; starting around 0.2 Hz, additional frequency content is present up to the signal frequency of 0.53 Hz. These irregularities are better observed in Fig. 7, which shows sample results of $T = 1.3s$. Labeled are the frequencies and corresponding amplitudes of the signal frequency, its second harmonic, and the new peak, which occurs around 0.266 Hz. One possible cause of this could be the excitation of the tank's
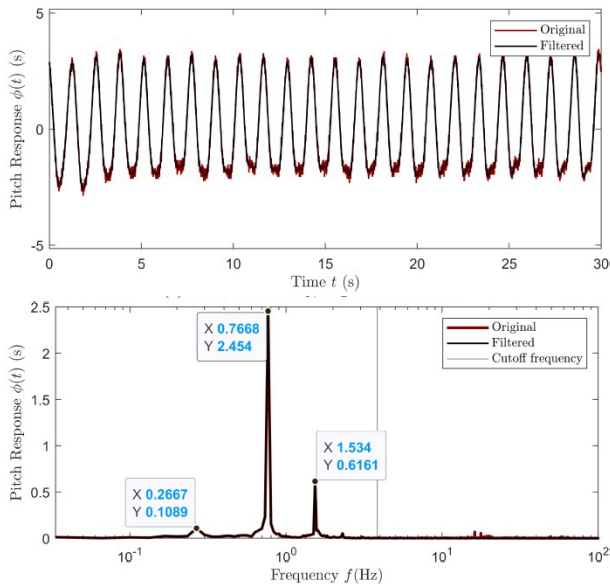

(a) Original (raw) time history

(b) FFT and filter frequency response

(c) Comparison of original and filtered signals

FIGURE 6 - Sample pitch response signal (no external springs, $T = 1.9$ s).

seiching natural period. For a rectangular basin, the seiching natural period is approximated by [25]

$$T_{n,seiche} = \frac{2L_t}{\sqrt{gh}} \tag{11}$$

where L_t is the length of the tank (basin). Given the ORRE tank length of 11.53 m, it has a seiching natural period of 7.36 s (0.136 Hz). The irregularity at 0.266 Hz could roughly correspond to the second seiching mode. Further, given that the tank is subdivided by the OSWEC, two other "basins" could be formed fore and aft of the model. These correspond to lengths of 4.91 m and 6.62 m and frequencies of 0.318 Hz and 0.237 Hz, respectively. Further analysis will be needed to verify the exact cause of this peak. The effect of these irregularities is evident in the corresponding time history, Fig. 7. Plotting the wave responses across all wave periods for both no spring and with spring cases reveal similar second-order harmonics except for at a period of $T = 2.0\ s$. A sample time history and FFT of the

8

configuration with external springs is provided in Fig. 8 for this period, which shows almost no higher harmonics.

FIGURE 7 - Sample pitch response with significant tank physics influence (no external springs, T = 1.3 s). (Top) Sliced time history, original and filtered. (Bottom) FFT signal.
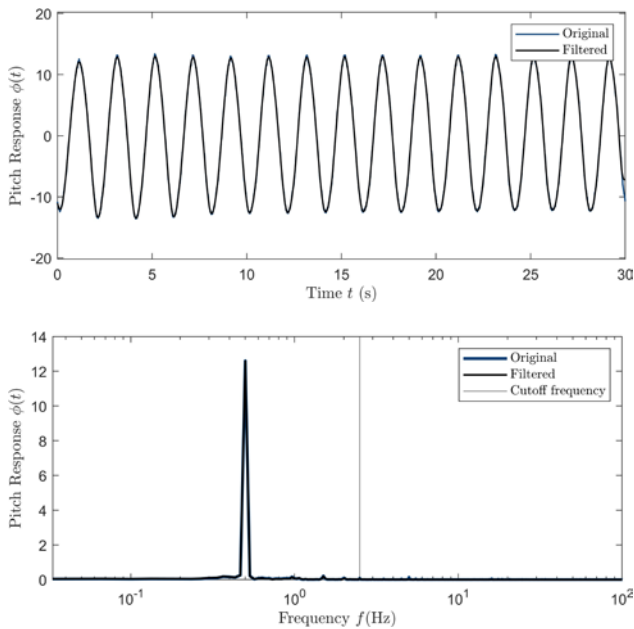

FIGURE 8 - Sample pitch response signal (**external springs**, T = 2.0 s). (Top) Sliced time history, original and filtered. (Bottom) FFT signal.

5. COMPARISON AND DISCUSSION

5.1 Pitch Response Amplitude Operator (RAO)

The response amplitude operator results are presented in Fig. 9. As anticipated, the response of the configuration with external springs near its natural period exceeds that of the OSWEC without springs. Normalized by amplitude, the non-dimensionalized RAO reveals the sharp peak characteristic of resonance at a period of around 2 s, higher than the anticipated natural period of 1.76 s. A similar yet smaller spike is also observed in the RAO of the configuration with no external springs at the same period of 2 s. The physical significance of this period is currently unknown. It might be due to the tank's seiching natural period and the second harmonics responses as discussed in the previous section. Further investigation is needed to understand the exact cause of response amplifying at this period. The pitch amplitude and RAO of the configuration with no external springs continues to climb toward the end of the observed period range.

Comparisons are also made with the results from the analytical model (Fig. 9). Except for the region near the 2.0 s period, overall, the theoretical solutions are shown to capture similar trends as the experimental data. In the no spring case, the RAOs are predicted to continue increasing toward the resonance region. In the external spring configuration, its values peak near the expected resonance period ($T \cong 1.75s$) and the motion amplitudes are estimated to decrease toward both ends of the frequency range. Some differences are noticed, including the smaller response outputs compared to experimental measurements across most frequencies from the analytical solutions. Since the analytical model is based on the linearity assumption, some differences due to neglecting nonlinearity are expected. Another reason for the variations could be due to the flat plate assumptions in calculating the added mass and
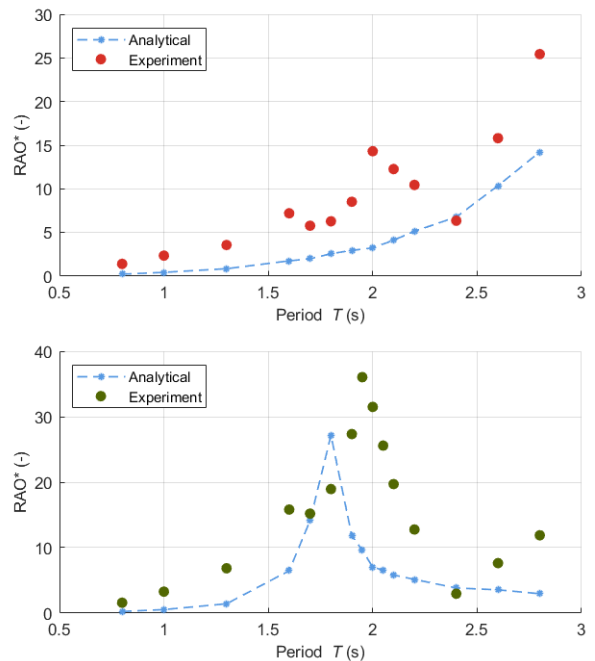

FIGURE 9 - Simulated response amplitude operator: (Top) no external springs and (Bottom) **external springs**.

9

radiation damping (Equations (17)-(22)). Their influence on the RAOs will be discussed in the next section. It is also noted here that the analytical solution correctly predicts the resonance at around 1.75 s, as measured in the free-decay tests.

5.2 Foundation Loads

The normalized amplitudes of the surge forces and the pitch reaction moment at the base of the foundation are plotted as a function of frequency in Figs 10 and 11. When normalized by wave amplitude, a bell-like curve, like that of a pitch response RAO, is observed. The peak loads in both cases (springs and without springs) occur at a 2-second period, as seen in the response. A drastic increase in loading is observed from the OSWEC configuration without springs to the configuration with springs. Near resonance, the surge force and pitch moment at the base of the external spring model are 20–30 times greater. Both force and moment drop drastically from 2.1 s to 2.4 s before rising again due to the increasing wave amplitude. For the no-spring configuration, after the first peak, the surge reaction force and pitch reaction moment increase slowly, tending toward the resonance frequency at around 4s. It is not shown here, but similar to the pitch response outcomes, higher harmonics are also recorded in the FFT loading results at twice the signal frequency.
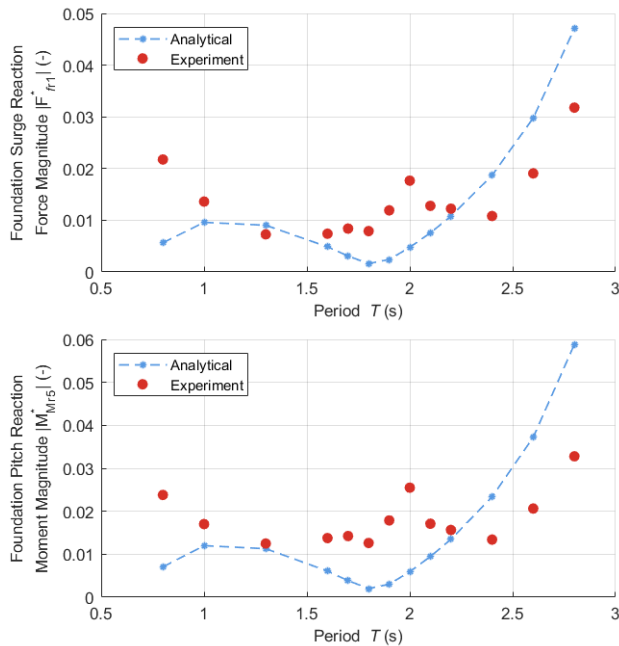
FIGURE 10 - Simulated foundation base reaction forces and moments, no external springs. The components are non-dimensionalized as $\left|F_{fr1}^*\right| = \left|F_{fr1}^*\right|/(\rho g h^2 a)$, $\left|M_{fr5}^*\right| = \left|M_{fr5}^*\right|/(\rho g h^2 a w)$.

The analytical model is also employed to evaluate the foundation surge forces and pitch moments. The results are presented together with experimental data in Figs 10 and 11. Except for the near resonance (1.75s to 2.0s) region, in which the

tank's physics might lead to differences in the results as discussed above, the theoretical solutions correlate relatively well with the measurements. Some differences are observed, including the small overestimate of analytical data in the no-spring case after the first peak and the underestimate of analytical predictions in the external spring set up. Similar to the RAO results, the reason for the variations could be due to the linearity and flat plate assumptions employed to estimate the hydrodynamic coefficients theoretically. A parametric study is carried out in the next section to investigate the sensitivity of these coefficients on the results.
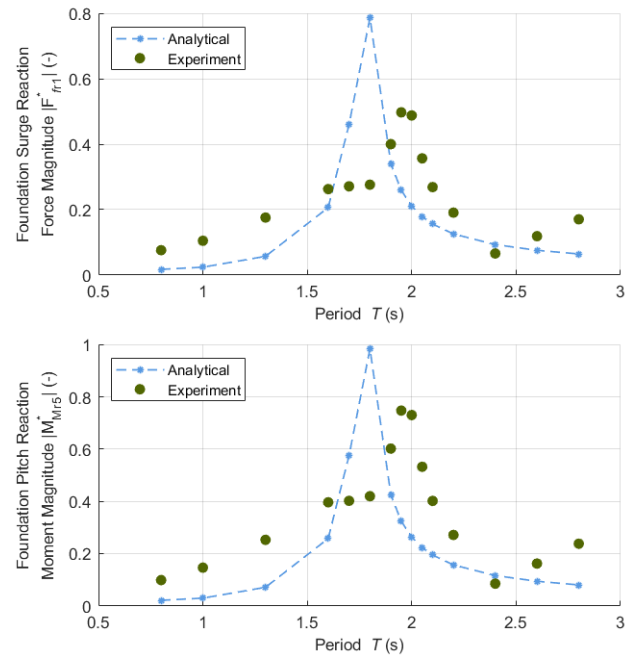
FIGURE 11 - Simulated foundation base reaction forces and moments, **external springs**. The components are non-dimensionalized as $\left|F_{fr1}^*\right| = \left|F_{fr1}^*\right|/(\rho g h^2 a)$, $\left|M_{fr5}^*\right| = \left|M_{fr5}^*\right|/(\rho g h^2 a w)$.

6.   PARAMETRIC STUDIES

This section examines the sensitivity of hydrodynamic coefficients on the RAOs and the foundation reaction surge forces. Pitch moments are not considered due to their similarity with the surge forces. From Equations (10) to (15), besides the geometric properties, it can be seen that A_{55}, A_{15}, B_{55}, and B_{15} are factors that could impact the key results listed above. The system natural period, however, depends on the values of A_{55}. As discussed previously, the analytical predictions of resonance are in good agreement with the results from decay test; the pitch added mass values therefore will not be varied. The parameterizations are carried out for the remaining components individually to assess their influences. Both cases without spring and with external springs are considered.

6.1 Response Amplitude Operator

From Equation (10), only the pitch radiation damping term B_{55} can influence the outputs of the RAOs, whereas A_{15} and B_{15} have no impact. For this study, the RAOs are estimated with B_{55} values varying from ($B_{55}, 1/2 \, B_{55}, 1/4 \, B_{55}$, and 0). The results are displayed in Fig. 12.

It is observed that in the no spring scenario, B_{55} has little to no influence on the RAO values. All the lines are shown to lie almost directly on top of each other. For the external spring setup, variations in B_{55} lead to small changes in the RAO values near resonance. As B_{55} decreases, the response amplitudes increase accordingly. Neglecting the differences in resonance period, the peak of the analytical outputs for the case of small B_{55} ($B_{55} \rightarrow 0$) show better agreement with the experimental data. The spread of the theoretical data, however, is observed to be smaller than those obtained from measurements. The impact of B_{55} is limited to the region around the resonance frequency. Outside this area, changes in B_{55} do not translate to variations in RAO values, and hence, the spread of the analytical curves remain compact.
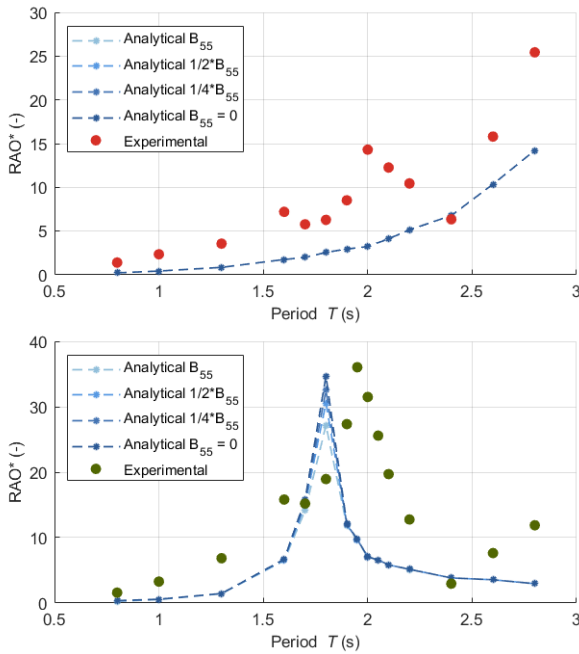
FIGURE 12 – Parameterizations of pitch radiation damping B_{55} and its influences on the RAOs. Top: no spring. Bottom: **external springs**. Experimental fit lines are second-order polynomial and 2-point moving average, respectively.
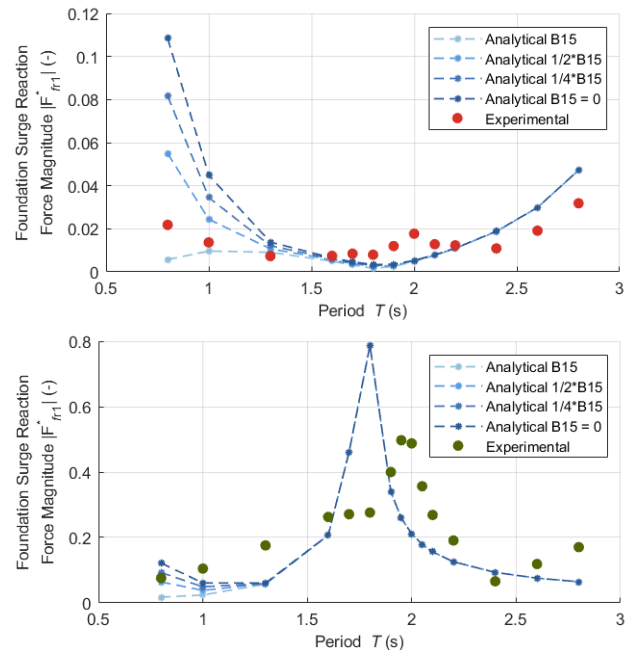
6.2 Hinge Reaction Surge Forces

Equation (15) shows that the reaction surge force depends directly on B_{15} and A_{15} values and indirectly on B_{55} through the response amplitudes. As discussed above, a decrease in B_{55} leads to small increase in the RAO peak near resonance. Outside this region, B_{55} has no impact on the results. For this reason, the parameterization in the following sections only examine the influences of B_{15} and A_{15} on the outputs.

6.2.1 Surge-Pitch Radiation Damping B_{15}

In this section, surge-pitch radiation damping values, B_{15}, are decreased gradually in a similar manner to B_{55} (with multiplication factor from 1, 1/2, 1/4, to 0) to examine the sensitivity of this parameter on the outputs. The results are shown in Fig. 13.

Both configurations - no springs, and external springs – show that variations of B_{15} are only reflected in the high frequency region ($T = 0.8s \, to \, 1.3s$). Outside this area, the differences between the outputs are negligible. While B_{15} values have little impact on the forcing in the external spring set up, the forces are observed to be highly sensitive to B_{15}'s variations in the high frequency region for the no spring case. As B_{15} gets larger, the surge forces in this region rises significantly.

FIGURE 13 – Parameterizations of surge-pitch radiation damping B_{15} and its influences on the hinge reaction forces. Top: no spring. Bottom: **external springs**.

6.2.2 Surge-Pitch Added Mass A_{15}

This section focuses on the sensitivity of the surge-pitch added mass on the forcing outputs. A_{15} values are varied with the multiplication factors ranging from 0.8 to 1.4 (no springs) and 0.6 to 1.4 (external springs). The results are presented in Fig. 14.

In the no-spring configuration, the experimental data are observed to correlate very well with the ($1.2 * A_{15}$) and ($0.8 * A_{15}$) curves before and after the peak at 2.0 s, respectively. It is noted that the added mass is frequency-dependent. The variables in this section, however, are parameterized using constant multipliers across all wave periods. It is reasonable that the

experimental data correlate to different curves in different frequency regions.

For the external spring set up, the forces are seen to increase monotonically as A_{15} values get larger. Aside from the near resonance (1.75 s to 2.0 s) region as previously discussed, the measured data are seen to correlate relatively well with the $(1.4 * A_{15})$ curve. Inside the near resonance region, without consideration for the shift in the resonance frequency due to the tank's physics, the forcing magnitudes could be seen to match closely with the $(0.6 * A_{15})$ line.

Further studies will be needed to validate the agreement between the analytical solutions and the experimental data employing different parameterization curves. The results in this section, however, show that while the flat plate assumptions could reasonably predict the OSWEC systems' responses and foundation forces within a very short time frame, incorporating the effects of plate thickness on the hydrodynamic coefficients can be important to improve the performance of the theoretical model.
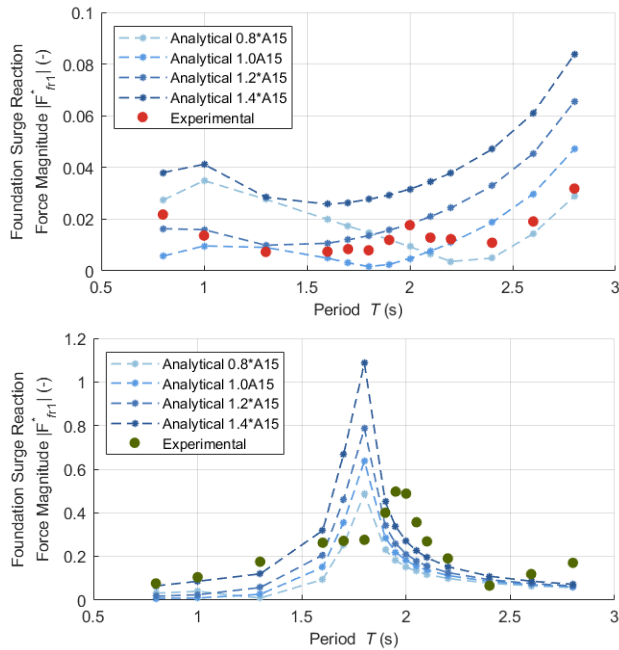
FIGURE 14 – Parameterizations of surge-pitch added mass A_{15} and its influences on the hinge reaction forces. Top: no spring. Bottom: **external springs**.

7. CONCLUSION

The paper seeks to investigate the performances and limitations of the analytical model of a bottom-raised OSWEC through experimental and parametric studies. The theoretical model was previously proposed to evaluate 1) the hydrodynamic coefficients of an OSWEC employing the flat plate assumption in elliptical coordinates, and 2) the corresponding RAOs, and foundational loadings/torques. An experimental campaign was carried out at the ORRE laboratory at University of Massachusetts Amherst to collect the experimental data. Two configurations of the model setup were employed: the OSWEC on its foundation with no additional attachments, and the OSWEC with additional torsional springs attached, to lower the natural period to within the range of periods producible by the tank's wave maker. Experimental runs were performed to identify the system dynamics and observe its response to regular first order waves. The OSWEC pitch angular displacement and reaction loads in surge, and pitch, measured at the base of the foundation, were reported in the frequency domain.

The analytical model was shown to capture the natural period of the two configurations well, but the pitch responses of both models appear to fall short of those observed in the experiments. The pitch response magnitudes of both models were about 50%-70% of the observations. The disparity persisted when the simulations were run without additional damping. A possible explanation for this discrepancy could be derived from tank physics; due to the tank's finite length, not modeled by the analytical methods, both wave reflection and seiching events can disrupt and modify the incident waves from the wavemaker. The differences between the two approaches could also be due to neglecting the thickness effects (flat plate assumption was employed in the analytical model) on the hydrodynamic coefficients. It is noted that while there are some differences in amplitudes, the analytical predictive curves follow similar trends to what were observed in the experimental data.

A parametric study was also conducted to examine the sensitivity of the hydrodynamic coefficients on the OSWEC's performances. For pitch RAOs, the impact of radiation damping B_{55} is observed to be small and limited to the region around resonance frequency. For surge foundational loads, while surge-pitch radiation damping B_{15} is shown to be one of the dominating factors in the low period (high frequency) region, surge-pitch added mass A_{15} is noticed to highly impact the results across the studied frequency range. A 20% decrease in this parameter is shown to reduce the peak loads up to 20%. This indicates that while the analytical model with the flat plate assumption could significantly reduce computational cost and reasonably predict the OSWEC's performance, incorporating the effects of plate thickness on the hydrodynamic coefficients can be an important factor in improving the model's accuracy.

REFERENCES

[1] Henry, A., 2009, *The Hydrodynamics of Small Seabed Mounted Bottom Hinged Wave Energy Converters in Shallow Water: PhD Thesis*, Queen's University Belfast.

[2] Henry, A., Rafiee, A., Schmitt, P., Dias, F., and Whittaker, T., 2014, "The Characteristics of Wave Impacts on an Oscillating Wave Surge Converter," J. Ocean Wind Energy, **1**(2), pp. 101–110.

[3] Renzi, E., Doherty, K., Henry, A., and Dias, F., 2014, "How Does Oyster Work? The Simple Interpretation of Oyster Mathematics," Eur. J. Mech. - BFluids, **47**, pp. 124–131.

[4] Whittaker, T., and Folley, M., 2005, "Optimisation of Wave Power Devices towards Economic Wave Power Systems," *World Renewable Energy Conference*.

[5] Whittaker, T., and Folley, M., 2012, "Nearshore Oscillating Wave Surge Converters and the Development of Oyster," Philos. Trans. R. Soc. Math. Phys. Eng. Sci.

[6] Tom, N. M., Lawson, M. J., Yu, Y. H., and Wright, A. D., 2016, "Development of a Nearshore Oscillating Surge Wave Energy Converter with Variable Geometry," Renew. Energy, **96**, pp. 410–424.

[7] Wei, Y., Rafiee, A., Henry, A., and Dias, F., 2015, "Wave Interaction with an Oscillating Wave Surge Converter, Part I: Viscous Effects," Ocean Eng., **104**, pp. 185–203.

[8] Wei, Y., Abadie, T., Henry, A., and Dias, F., 2016, "Wave Interaction with an Oscillating Wave Surge Converter. Part II: Slamming," Ocean Eng., **113**, pp. 319–334.

[9] Renzi, E., and Dias, F., 2013, "Hydrodynamics of the Oscillating Wave Surge Converter in the Open Ocean," Eur. J. Mech. - BFluids, **41**, pp. 1–10.

[10] Babarit, A., Hals, J., Muliawan, M. J., Kurniawan, A., Moan, T., and Krokstad, J., 2012, "Numerical Benchmarking Study of a Selection of Wave Energy Converters," Renew. Energy, **41**, pp. 44–63.

[11] Newman, J. N., 1977, *Marine Hydrodynamics*, MIT Press, Cambridge, Mass.

[12] Falnes, J., 2002, *Ocean Waves and Oscillating Systems: Linear Interactions Including Wave-Energy Extraction*, Cambridge University Press, Cambridge.

[13] Korde, U. A., and Ringwood, J., 2016, *Hydrodynamic Control of Wave Energy Devices*, Cambridge University Press.

[14] US Department of Energy - Office Of Energy Efficiency & Renewable Energy, "Technology Commercialization Fund," Energy.gov [Online]. Available: https://www.energy.gov/eere/solar/technology-commercialization-fund. [Accessed: 06-Jan-2022].

[15] Renzi, E., and Dias, F., 2012, "Resonant Behaviour of an Oscillating Wave Energy Converter in a Channel," J. Fluid Mech., **701**, pp. 482–510.

[16] Nguyen, N., Davis, J., Thiagarajan, K., Tom, N., and Burge, C., "Optimizing Power Generation of a Bottom-Raised Oscillating Surge Wave Energy Converter Using a Theoretical Model," p. 9.

[17] Davis, J., 2021, "Design and Testing of a Foundation Raised Oscillating Surge Wave Energy Converter," Masters Theses.

[18] Techet, A.H., 2005. 13.42 Design Principles for Ocean Vehicles.

[19] Gomes, R.P.F., Lopes, M.F.P., Henriques, J.C.C., Gato, L.M.C. and Falcão, A.F.O., 2015. The dynamics and power extraction of bottom-hinged plate wave energy converters in regular and irregular waves. *Ocean Engineering*, **96**, pp.86-99.

[20] Kurniawan, A. and Moan, T., 2012. Characteristics of a pitching wave absorber with rotatable flap. *Energy Procedia*, *20*, pp.134-147.

[21] Inman, D.J., 2008. Engineering vibration. Upper Saddle.

[22] McCormick, M.E., 2007. Ocean Wave Energy Conversion Dover Publication Inc. *Chapter 4*.

[23] Chakrabarti, S.K., 1994. *Offshore structure modeling* (Vol. 9). world scientific.

[24] Fontana, M., Casalone, P., Sirigu, S.A., Giorgi, G., Bracco, G. and Mattiazzo, G., 2020. Viscous damping identification for a wave energy converter using CFD-URANS simulations. *Journal of Marine Science and Engineering*, *8*(5), p.355.

[25] Dean, R.G. and Dalrymple, R.A., 1991. *Water wave mechanics for engineers and scientists* (Vol. 2). world scientific publishing company.